



Buckling delamination in compressed multilayers on curved substrates with accompanying ridge cracks

S. Faulhaber^a, C. Mercer^a, M.-W. Moon^b,
J.W. Hutchinson^{b,*}, A.G. Evans^a

^a*Materials Department, University of California, Santa Barbara, CA 93106, USA*

^b*Division of Engineering and Applied Sciences, Harvard University, Cambridge, MA 02138, USA*

Received 3 August 2005; received in revised form 7 November 2005; accepted 19 November 2005

Abstract

Residually compressed films and coatings are susceptible to buckle delamination. The buckles often have linear or telephone cord morphology. When the films are brittle, such buckles are susceptible to the formation of ridge cracks that extend along their length, terminating close to the propagating front. The ridge-cracked buckles are invariably straight-sided (not telephone cord) and differ in width. Buckle delaminations of this type occur on flat and curved substrates: having greatest technological relevance in the latter. They occur not only in single layer films but also in multilayers, such as thermal barrier systems. Establishing the mechanics of ridge-cracked buckle delaminations for multilayers on curved substrates serves two purposes. (a) It allows the prediction of buckle delamination and spalling for technologically important systems. (b) It provides a test protocol for measuring properties such as the delamination toughness of the interface and the stresses in the layers. Both objectives are addressed in the article: the latter by devising an inverse algorithm. Implementation of the algorithm is demonstrated for diamond-like carbon films on planar glass substrates and a thermal barrier multilayer on a curved superalloy substrate.

© 2005 Elsevier Ltd. All rights reserved.

Keywords: Thermal barrier coatings; Delamination; Curved substrates; Interface toughness; Inverse problem

*Corresponding author.

E-mail address: Hutchinson@husm.harvard.edu (J.W. Hutchinson).

Nomenclature

a	ridge-crack length
b	buckle half-width
b_0	reference half-width of buckle on flat substrate at onset of buckling
h_i	thickness of i th layer
h_T	total thickness of multilayer
u	tangential displacement in x -direction at $y = y_0$
w	displacement normal to the substrate
D	bending stiffness of multilayer
E_i	Young's modulus of i th layer (isotropic, elastic)
\bar{E}	plane strain modulus [$E/(1 - \nu^2)$]
J	number of layers in multilayer film
G_T	total energy/area released upon delamination (bending and stretching)
G_{side}	energy release rate at sides of delamination
G_{ss}	energy release rate under steady-state propagation at front of delamination
G_0	stretching energy/area released upon delamination (without bending)
M_0	residual bending moment/length
\hat{M}_0	normalized residual bending moment/length
N_0	pre-buckling force/length (positive in compression)
ΔN_{xx}	additional resultant force/length
R	radius of substrate of cylindrical substrate
S	stretching stiffness of multilayer
ΔU	change in elastic energy/length
α	rotation at ridge crack, $\alpha \equiv w'(b)$
δ	buckling deflection amplitude, $\delta \equiv w(b)$
$\varepsilon_{\alpha\beta}^0$	initial residual strains
$\Delta\varepsilon_{\alpha\beta}$	additional strains
λ	dimensionless curvature ($\lambda = Sb^4/DR^2$)
λ_0	dimensionless curvature ($\lambda_0 = Sb_0^4/DR^2$)
ν_i	Poisson's ratio of i th layer
$\Delta\sigma_{\alpha\beta}$	additional stress
$\sigma_{\alpha\beta}^0(y)$	in-plane residual stress of layer (dependent on y)
ψ	mode mix [$\arctan(K_{II}/K_I)$]

1. Introduction

An increasing number of technologically important systems comprise thin multilayers on non-planar substrates. The layers, which serve multiple purposes, are exemplified by two illustrations. (i) Thermal protection systems used in aero-propulsion and space re-entry, which impart thermal and oxidation protection functionalities (Fig. 1) (Clarke and Levi, 2003; Levi, 2004; Evans et al., 2001; Stiger et al., 1999). (ii) Diamond-like carbon (DLC) films, which impart tribological benefits to hard surfaces (Fig. 2, Moon et al., 2002a). To inhibit cracking, these layers are designed to be in compression at their

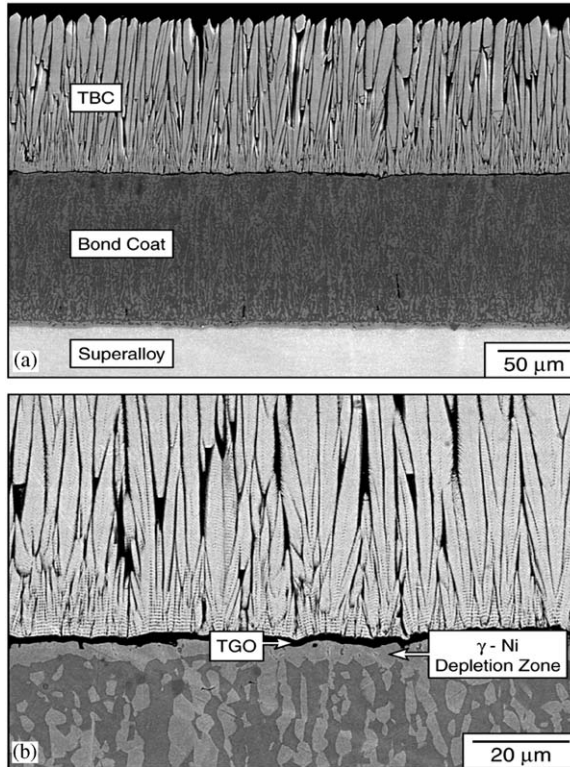


Fig. 1. An image of a tri-layer thermal barrier system for gas turbines comprising an yttria-stabilized zirconia (YSZ) insulating top layer, an alumina interlayer and a Ni alloy bond coat (the substrate is not shown) (Evans et al., 2001).

operating temperatures. This is achieved by the appropriate choices of deposition method and thermal expansion misfit. However, compressed layers are susceptible to buckling induced delamination (Figs. 2a–e). The phenomenon is prevalent when the residual compression is large and the interface has low delamination toughness (Freund and Suresh, 2004). Solutions relating the extent of delamination to the stress and the interface toughness have been found for thin (uncracked) single layer films on flat substrates (Hutchinson and Suo, 1992), and validated by comparison with measurements. More recently, the solutions have been extended to include single layer films on curved substrates (Hutchinson, 2001), as well as to buckles with telephone cord (not just straight-sided) morphology (Moon et al., 2002b; Lee et al., 2004).

After buckling, when the films are brittle, the induced bending causes the top of the film to experience large enough tensile stress that ridge cracks develop (Fig. 2d). When this happens, the buckles tend to be straight-sided (rather than telephone cord) and the cracks typically extend almost to the front (within a buckle half-width, b). Such ridge-cracking affects the energy release rate and the mode mixity, resulting in different delamination tendencies, as evident from Fig. 2d. A preliminary analysis of these effects for a single layer film has been presented by Thouless (1993). A more comprehensive analysis will be developed in the present article.

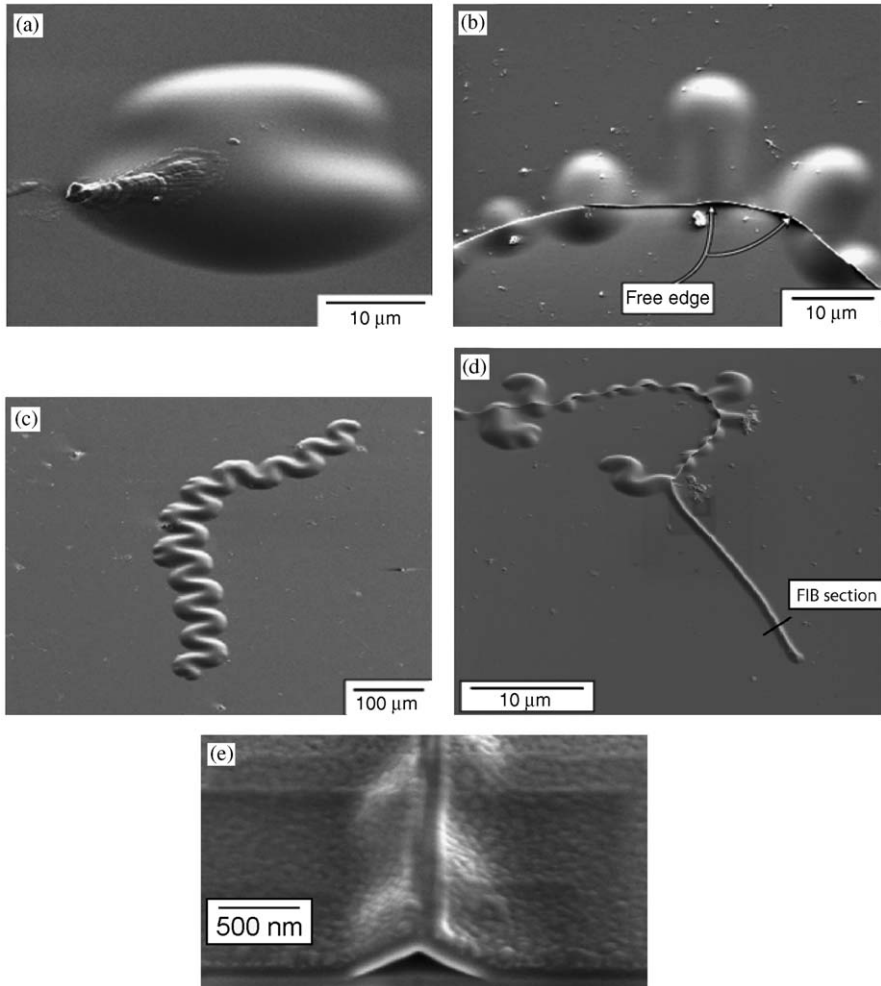


Fig. 2. (a–c) Examples of buckle delaminations observed in a system comprising a thin DLC film on a glass substrate (Moon et al., 2002a). (d) An example of two competing buckle delamination morphologies. One is the telephone cord and the other is a straight-sided buckle with a ridge crack that extends to within a buckle width of the front. Note that the ridge-cracked buckle is narrower than the telephone cord. (e) A FIB cross-section through the buckle with the ridge crack. The film used to illustrate the inverse algorithm in Section 4.1 is roughly three times thicker than that shown here.

The ridge-cracking phenomenon also exists in multilayer films on both flat and curved substrates, such as thermal barrier systems. Observations conducted on these systems, which will be presented in Section 2, motivate the mechanics to be described in Section 3. The mechanics has dual objectives: (a) To reveal the role of ridge cracks on the energy release rates of straight-sided delaminations on flat and curved substrates. (b) To infer unknown properties from experimental measurements of the deflection amplitude and width of a buckle delamination. This inverse problem, while straightforward for a straight-sided delamination on a flat substrate (absent a ridge crack), becomes increasingly difficult in the presence of cracks and when the substrate is curved. Nevertheless, an inverse

algorithm has been identified and will be demonstrated. Its application to DLC films and thermal barrier systems will be presented in Section 4.

One of the remarkable findings of this investigation is that the inverse algorithm can be used to infer two properties simultaneously. Specifically, when the elastic properties of the layers are known, *both the residual film stress and interface toughness* can be obtained. Alternatively, if the stress is known, *the modulus and interface toughness* can be ascertained. The latter is especially relevant for thermal barrier systems.

2. Observations on thermal barrier systems

2.1. The concept

Thermal barrier systems comprise bi-layers of yttria-stabilized zirconia (YSZ) and a thermally grown oxide (TGO, typically alumina), attached to a bond coat, located (in turn) on a superalloy substrate. We address a system with a NiCoCrAlY bond coat, which buckles by delamination along the TGO/bond coat interface (Fig. 3) (Xu et al., 2004). To predict the incidence of delamination, direct assessment of the mode II toughness of this interface is needed, as well as its dependence on time/cycle exposure. The focus of this assessment is on the use of buckle/delamination to obtain such measurements. For this purpose, a cylindrical thermal barrier system is impressed with a wedge indenter to induce axial, straight-sided buckles, with ridge cracks (Fig. 4).

2.2. The material

The specimens consist of cylinders, radius $R = 6$ mm, coated over ~ 64 mm of their length (Xu et al. 2004). The bond coat consists of Ni-22Co-17Cr-12.5Al-0.25Hf-0.4Si-0.6Y (wt%). The thermal barrier coating (TBC) layer has thickness, $h_{\text{tbc}} = 140$ μm , deposited by rotating in an electron beam physical vapor deposition system. It has a columnar structure with ~ 4 μm diameter grains. A burner rig test was used to expose the specimens to thermal cycles comparable to those expected on the first-stage airfoils in a gas turbine. The apparatus consists of an anchor plate that rotates and also translates vertically relative to a high-velocity flame. The vertical movement translates the specimens in and out of the

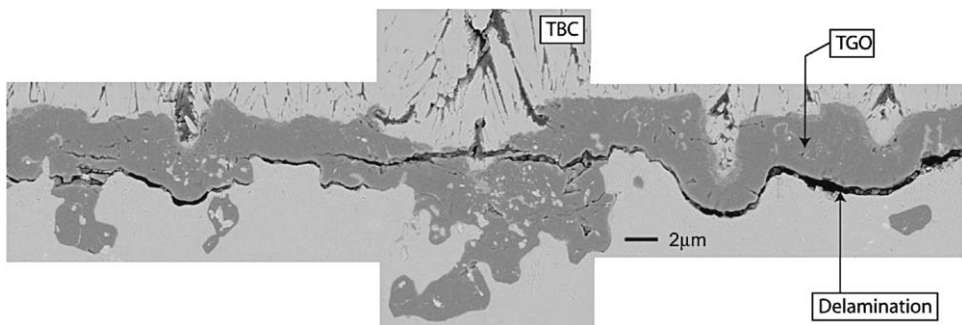


Fig. 3. A delamination in a thermal barrier system (Xu et al., 2004) showing that its trajectory is along the TGO/bond coat interface.

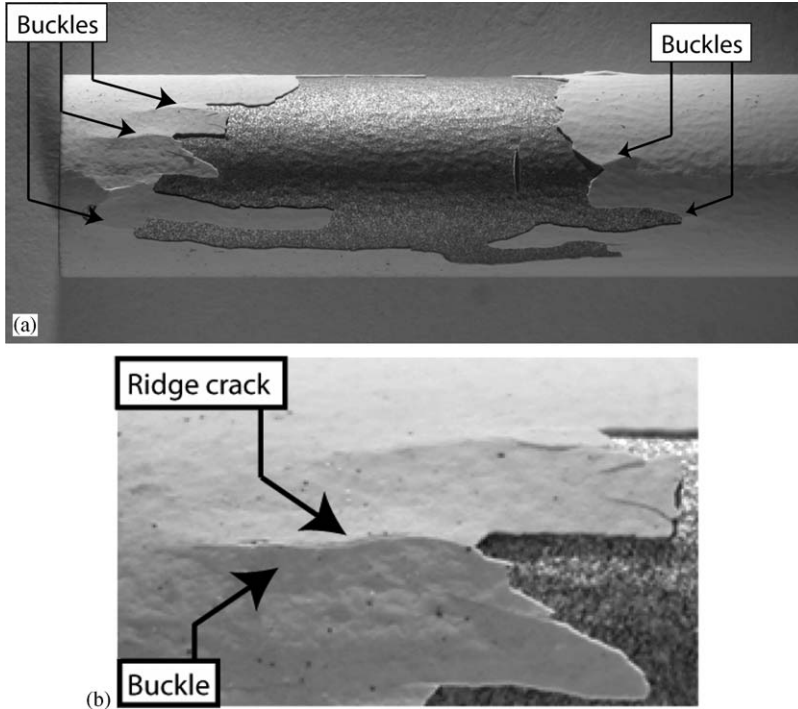


Fig. 4. A region of a partially spalled TBC bilayer showing straight-sided buckles with a ridge crack in the region ahead of the spall. Note that the linear regions of the spall have the same width as the buckle.

flame, at a rate that determines the time-at-temperature and the overall cycle time. Each cycle comprises a rapid heat up (15 s), 5 min exposure at temperature, and a rapid cool down with forced air for 90 s. A series of specimens were tested to various fractions of the nominal life. At full life, the TGO had average thickness, $h_{\text{TGO}} = 2.3 \mu\text{m}$.

2.3. Wedge tests

A wedge indenter with an included angle of 90° was used to impress through the TBC/TGO bilayer normal to the cylinder axis. This was achieved by attaching the indenter to the cross head of a hydraulic test frame. The load was systematically elevated until the wedge penetrated the bond coat. It was then removed. In all of the thermally cycled specimens, substantial regions of the thermal barrier spalled (Fig. 4). More importantly, beyond the spall, several linear, axial buckles were created. Each had similar width, $2b$, and all were accompanied by ridge cracks that extend to within b of the front. The buckles have been examined in further detail.

Cross-sections were made through the buckles in the ridge-cracked region (remote from the front), by grinding and polishing, utilizing a precision polishing system to maintain flatness. Micro-cloth with multi-crystalline diamond spray ($3 \rightarrow 1 \rightarrow 0.25 \mu\text{m}$) was used for final polishing to preserve the fine structure without distortion. After sectioning, the specimens were characterized using field-emission scanning electron microscopy (FE-SEM). Typical images are presented on Fig. 5. These observations reveal, among other

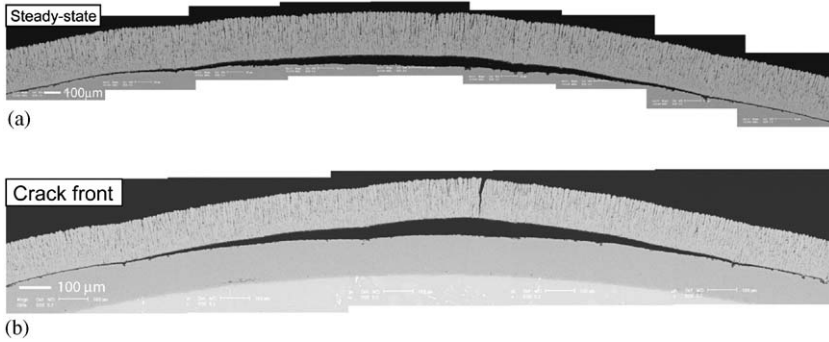


Fig. 5. Images of two cross-sections from the buckles depicted in Fig. 4. (a) The steady-state ridge-crack region showing that the crack extends through the TBC layer but stops at the TGO, resulting in a hinge around the intact TGO. (b) A corresponding region just ahead of the ridge crack, near the propagating front.

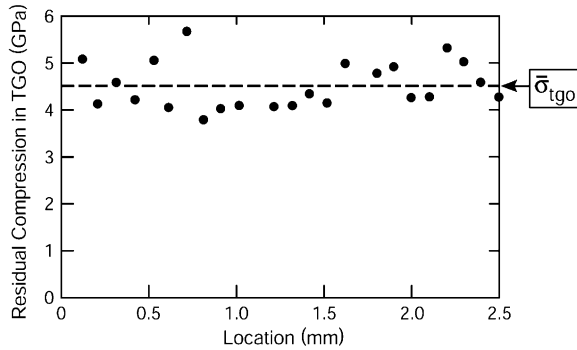


Fig. 6. Variations in the residual compression in the TGO measured using photo-stimulated luminescence spectroscopy.

factors, that the ridge cracks extend through the YSZ layer, leaving the TGO layer intact. That is, the crack hinges at the base of the bilayer, with implications for the pursuant mechanics.

For the samples examined, the relevant dimensions are: $b = 1.2$ mm, $\delta = 60.8$ μm , $\alpha = 2.6^\circ$ (here b is the buckle half width, δ is the height of the buckle above the substrate surface and α is the included angle, see Fig. 7). These measurements are used in Section 4 to assess the interface toughness, as well as the unknown modulus of the TBC. The latter determination becomes feasible subject to independent knowledge of the residual stresses in the TGO, described next.

2.4. Stress measurements in the TGO

Photo-stimulated luminescence spectroscopy (PSLS) allows determination of the stress from the shift in frequency originating from luminescent ions incorporated in a material. In its application to measurement of the ambient residual stress in a TGO, the luminescence is in the red (~ 690 nm) and comes from Cr^{3+} ions incorporated in the

alumina formed on the bond coat during high temperature exposure (Ma and Clarke, 1993). Details of the technique and its implementation can be found elsewhere (Ma and Clarke, 1993; Lipkin and Clarke, 1996). The method has been used to measure the stress in the TGO in an intact region, where it is attached to substrate. The results from a typical scan are presented in Fig. 6, indicating a stress, $\sigma_{\text{TGO}} = -4.4 \pm 0.67$ GPa.

3. Delamination energy release rates

The outline of this section is as follows:

- (i) A general formulation governing delamination of multilayer films.
- (ii) Solutions for *substrates without ridge cracks*: (a) flat substrates (including the inverse problem), (b) curved substrates and (c) necessary condition for the initiation of ridge cracks.
- (iii) Extension to flat and curved substrates *with ridge cracks*: (a) effects of ridge cracks and residual moment for flat substrates and (b) effects of ridge cracks and residual moment for curved substrates.
- (iv) The inverse algorithm.

3.1. General formulations governing multilayer buckling

Consider a multilayer film on a flat ($R \rightarrow \infty$) or cylindrical substrate that undergoes a straight-sided buckling delamination of width $2b$ (Fig. 7). The coordinate system has the origin of the y -axis at the interface with the substrate, where separation occurs, with x the arc length measured from the left end of the delamination. The film has J layers, thickness h_j ($j = 1, J$), counting from the interface: the total thickness is denoted by h_T . Each layer is assumed to be isotropic and elastic, with modulus E_j and Poisson's ratio ν_j . The in-plane residual stresses in the unbuckled film are denoted by $\sigma_{\alpha\beta}^0(y)$, which may vary with y from layer to layer and even within a given layer.

(i) *The deformation of the film* from the unbuckled state is represented using Donnell–Mushtari–Vlassov (DMV) theory for nonlinear behavior of shallow shells. In effect, the film is regarded as a curved wide beam clamped along its sides. The clamped condition is valid as long as the substrate modulus is not less than about one third that of the film (Parry et al., 2005). DMV reduces to the von Karman plate theory for an initially flat film. The bending and stretching strains from DMV theory relevant to the analysis of straight-sided buckle delaminations are

$$K_{xx} = w'' \quad \text{and} \quad E_{xx} = u' + \frac{w}{R} + \frac{1}{2}w'^2. \quad (1)$$

Here, E_{xx} , measures the strain at $y = y_0$, where y_0 will be identified below; w is the displacement normal to the substrate; u is the tangential displacement in the x -direction at $y = y_0$; $(\prime) = d()/dx$. These are the *additional strains* measured from the unbuckled state and do not include the initial residual strains, $\varepsilon_{\alpha\beta}^0$ (which will be accounted for below). At any point through the thickness of the film the additional strain in the x -direction is given by $\Delta\varepsilon_{11} = E_{xx} - (y - y_0)K_{xx}$.

(ii) *The change in energy arising from buckling of the film.* Attention is focused on a representative section well behind the propagating delamination front, where deformations

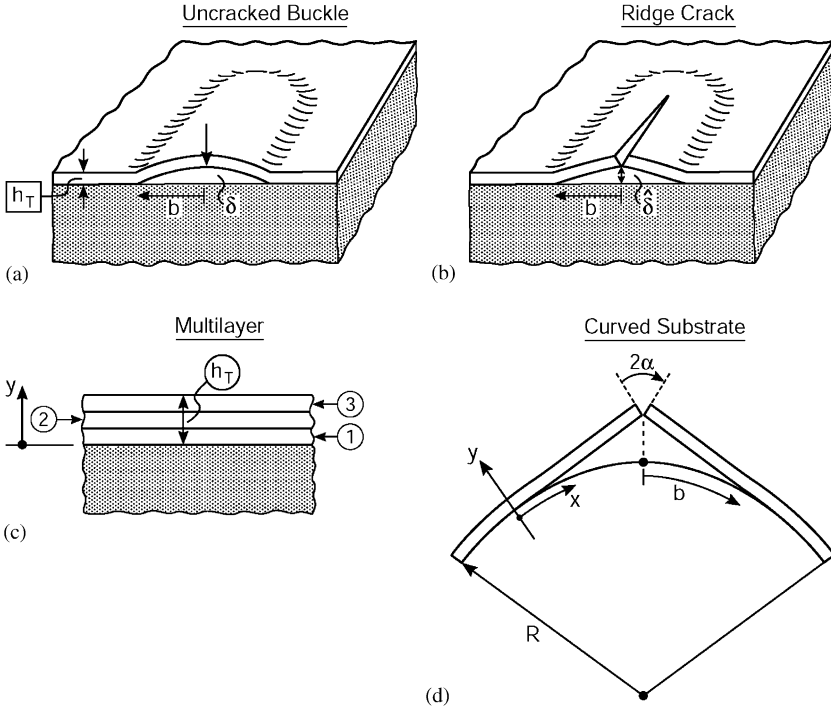


Fig. 7. Geometry of straight-sided buckling delaminations with and without ridge cracks.

satisfy the plane strain constraint, $\Delta\epsilon_{33} \equiv \Delta\epsilon_{zz} = 0$. It follows that the elastic energy density at any point in the film in the buckled state is

$$\begin{aligned} \frac{1}{2} \sigma_{\alpha\beta} \epsilon_{\alpha\beta} &= \frac{1}{2} \sigma_{\alpha\beta}^0 \epsilon_{\alpha\beta}^0 + \sigma_{\alpha\beta}^0 \Delta\epsilon_{\alpha\beta} + \frac{1}{2} \Delta\sigma_{\alpha\beta} \Delta\epsilon_{\alpha\beta} \\ &= \frac{1}{2} \sigma_{\alpha\beta}^0 \epsilon_{\alpha\beta}^0 + \sigma_{11}^0 \Delta\epsilon_{11} + \frac{1}{2} \Delta\sigma_{11} \Delta\epsilon_{11}, \end{aligned} \tag{2}$$

where $\Delta\sigma_{\alpha\beta}$ denotes the additional stress. Let ΔU denote the change in elastic energy (per unit length in the z -direction) in the film from the unbuckled to the buckled state. By DMV theory

$$\begin{aligned} \Delta U &= \iint \left(\sigma_{11}^0 \Delta\epsilon_{11} + \frac{1}{2} \Delta\sigma_{11} \Delta\epsilon_{11} \right) dy dx \\ &= \int_0^{2b} \left\{ -N_0 E_{xx} - M_0 K_{xx} + \frac{1}{2} S E_{xx}^2 + \frac{1}{2} D K_{xx}^2 \right\} dx, \end{aligned} \tag{3}$$

where y_0 has been chosen such that

$$y_0 \int_0^{h_T} \bar{E} dy = \int_0^{h_T} \bar{E} y dy \tag{4}$$

with $\bar{E} = E/(1 - \nu^2)$. In addition, N_0 is the resultant pre-buckling stress (force/length) defined to be positive in compression with

$$N_0 = - \int_0^{h_T} \sigma_{11}^0 dy. \tag{5}$$

The residual bending moment about y_0 in the unbuckled film is (per length):

$$M_0 = \int_0^{h_T} \sigma_{11}^0 (y - y_0) dy. \tag{6}$$

With this definition, a multilayer with compressive pre-stress at the bottom and tension at the top has positive M_0 . The stretching stiffness, S , and bending stiffness, D , of the multilayer are defined by

$$S = \int_0^{h_T} \bar{E} dy \quad \text{and} \quad D = \int_0^{h_T} \bar{E} (y - y_0)^2 dy. \tag{7}$$

(iii) *The buckle shape.* Clamped boundary conditions at the sides of the delamination require $u = w = w' = 0$ at $x = 0$. For the buckled film *with no ridge crack*, symmetry dictates that $u = w' = w''' = 0$ at $x = b$. The displacements of the beam in the buckled state are obtained from minimization of the elastic energy. The governing equations are obtained from the variational problem, $\delta \Delta U = 0$ for all admissible variations δu and δw . One outcome is that the additional resultant stress, $\Delta N_{xx} = S E_{xx}$, is independent of x . Thus, the compressive resultant stress in the buckled film, $N \equiv N_0 - \Delta N_{xx}$, is also independent of x . The moment equilibrium equation governing the normal deflection is

$$Dw'''' + N(w'' - R^{-1}) = 0. \tag{8}$$

This equation is supplemented by the requirements $u(0) = 0$ and $u(b) = 0$. The problem is fully specified in terms of the boundary conditions. The residual moment, M_0 , does not enter the problem and has no influence on either the buckled shape or the energy release rates.

For *the cracked film*, the crack has been assumed to extend almost entirely through the film, such that it can be modeled as a hinge located at the bottom (see Fig. 9 in Section 3.2). Then, with $u(b) = -\alpha y_0$ (where $\alpha \equiv w'(b)$ is the rotation at the ridge crack: Fig. 7), integrating the expression for E_{xx} from 0 to b gives:

$$\frac{b(N_0 - N)}{S} = \frac{1}{2} \int_0^b w'^2 dx + R^{-1} \int_0^b w dx - \alpha y_0, \tag{9}$$

where αy_0 is the contribution from the ridge crack. The boundary conditions at the center of the film at the location of the ridge crack emerge from the variational problem, given the hinge constraint $\delta u = -y_0 \delta w'$ at $x = b$. The conditions are found to be

$$Dw'' = M_0 - y_0 N \quad \text{and} \quad Dw''' + Nw' = 0 \quad \text{at } x = b. \tag{10}$$

The first states there is no net moment about the hinge at the bottom of the crack. The second is the condition that the transverse shear force vanishes at the center of the delamination (which also pertains to the uncracked film). The residual moment makes its presence felt through the first condition in Eq. (10).

3.2. General formulae for the energy release rates

Two reference quantities will be used throughout:

$$G_0 = \frac{N_0^2}{2S}, \quad b_0 = \pi \sqrt{\frac{D}{N_0}}, \quad (11)$$

where G_0 is the elastic energy/area stored in the multilayer that can be released by plane strain stretch alone (no bending); b_0 is the half-width of the delaminated region associated with the onset of buckling of the multilayer on a flat substrate.

At the *sides of the delamination*, well behind the curved front, the energy release rate can be expressed in terms of the change in curvature and resultant stress at the sides according to (Hutchinson and Suo, 1992)

$$G_{\text{side}} = \frac{(N_0 - N)^2}{2S} + \frac{1}{2} D w''(0)^2. \quad (12)$$

The energy release rate *averaged over the curved front* under steady-state propagation is given by

$$G_{\text{ss}} = \frac{-\Delta U}{2b}, \quad (13)$$

where ΔU is given by Eq. (3).

Another quantity of interest is the *total energy/area released when the film is set free from the substrate* (subject to plane strain stretching and bending):

$$G_{\text{T}} = \frac{N_0^2}{2S} + \frac{M_0^2}{2D} = G_0(1 + (\hat{y}_0 \hat{M}_0)^2). \quad (14)$$

Attention will be limited to systems with convex curvature, $R > 0$. The four dimensionless parameters characterizing the system are

$$\hat{y}_0 = y_0 \sqrt{\frac{S}{D}}, \quad \hat{M}_0 = \frac{M_0}{N_0 y_0}, \quad \frac{b}{b_0}, \quad \lambda = \frac{Sb^4}{DR^2}. \quad (15)$$

Other dimensionless combinations include

$$\frac{b^2}{Ry_0} = \frac{\sqrt{\lambda}}{\hat{y}_0}, \quad \frac{M_0 b^2}{Dy_0} = \pi^2 \hat{M}_0 \left(\frac{b}{b_0}\right)^2, \quad \lambda_0 \equiv \frac{Sb_0^4}{DR^2} = \left(\frac{b_0}{b}\right)^4 \lambda. \quad (16)$$

Note that $\hat{y}_0 = \sqrt{3}$ for a uniform single layer film; the normalized residual bending moment, \hat{M}_0 , only comes into play for ridge-cracked films.

3.3. Flat and curved substrates without ridge cracks

3.3.1. Delamination on flat substrates

While the results for this case are well known for single layer films (Hutchinson and Suo, 1992), it had not been previously noted that the energy release rates and the pre-stress can be expressed in an elementary and remarkably simple way in terms of the width of the delamination and the buckling deflection amplitude, $\delta \equiv w(b)$: not only for single layer films but also for multilayers. The results are obtained directly from the equations cited above without approximation. They are quoted without derivation because the solution

steps are considerably simpler than for more complicated cases described later:

$$\begin{aligned} G_{\text{side}} &= \frac{1}{2} S \left(\frac{\pi \delta}{4b} \right)^4 + 2D \left(\frac{\pi}{b} \right)^2 \left(\frac{\pi \delta}{4b} \right)^2, \\ G_{\text{ss}} &= \frac{1}{2} S \left(\frac{\pi \delta}{4b} \right)^4, \\ N_0 &= D \left(\frac{\pi}{b} \right)^2 + S \left(\frac{\pi \delta}{4b} \right)^2. \end{aligned} \quad (17)$$

Thus, if S and D are known and the buckling amplitude and delamination width are measured, the above equations can be used to evaluate the energy release rates and the resultant pre-stress. The two energy release rates are also given in the more familiar form:

$$\begin{aligned} \frac{G_{\text{side}}}{G_0} &= \left(1 - \left(\frac{b_0}{b} \right)^2 \right) \left(3 + \left(\frac{b_0}{b} \right)^2 \right), \\ \frac{G_{\text{ss}}}{G_0} &= \left(1 - \left(\frac{b_0}{b} \right)^2 \right)^2 \end{aligned} \quad (18)$$

with

$$\left(\frac{b}{b_0} \right)^2 = \frac{N_0}{N} \quad \text{and} \quad \frac{\delta}{y_0} = \frac{4}{\hat{y}_0} \sqrt{\left(\frac{N_0}{N} - 1 \right)}.$$

These also apply to both single layer and multilayer films. As stated earlier, the residual moment, M_0 , has no influence on the results.

3.3.2. Delamination on curved substrates without ridge cracks

Elementary expressions, such as those given above for flat substrates, do not appear to exist for curved substrates. The solutions can be obtained in closed form, but the resulting set of equations governing δ , N , etc. are nonlinear, coupled and implicit. These have been presented previously for single layer films (Hutchinson, 2001). They will be quoted here without derivation in a form valid for both single films and multilayers. From Eq. (8), the amplitude of the normal deflection is

$$\frac{\delta}{y_0} = \frac{b^2}{Ry_0} \left[\frac{1}{p \sin p} (1 - \cos p) - \frac{1}{2} \right], \quad (19)$$

where (anticipating $N > 0$)

$$p \equiv \sqrt{\frac{N}{D}} b = \pi \frac{b}{b_0} \sqrt{\frac{N}{N_0}}. \quad (20)$$

Condition (9) with $\alpha = 0$ becomes

$$1 - \frac{N}{N_0} = \frac{\lambda_0}{\pi^2} \left(\frac{b}{b_0} \right)^2 \left\{ -\frac{1}{6} + \frac{1}{4} \frac{1}{(\sin p)^2} \left(1 - \frac{\sin 2p}{2p} \right) \right\}. \quad (21)$$

Eq. (21) is transcendental for N/N_0 , in terms of b/b_0 and λ_0 . The energy release rates are

$$\frac{G_{\text{side}}}{G_0} = \left(1 - \frac{N}{N_0}\right)^2 + \frac{\lambda_0}{\pi^4} \left(1 - \frac{p}{\tan p}\right)^2, \tag{22}$$

$$\frac{G_{\text{ss}}}{G_0} = 1 - \left(\frac{N}{N_0}\right)^2 + \frac{\lambda_0}{\pi^4} \left(1 - \frac{1}{2} \left(\frac{p}{\sin p}\right)^2 \left(1 + \frac{\sin 2p}{2p}\right)\right). \tag{23}$$

The limit for the flat substrate has $p \rightarrow \pi$ as $R \rightarrow \infty$; it is simplest to obtain the results listed in Eqs. (17)–(18) starting directly with the equations for $R = \infty$.

Plots of the energy release rates as a function of b/b_0 are given in Fig. 8 for several values of λ , including the limit for the flat substrate. For each point on the plot, N/N_0 (and p) are determined from Eq. (21) and the energy release rates evaluated using Eqs. (22) and (23).

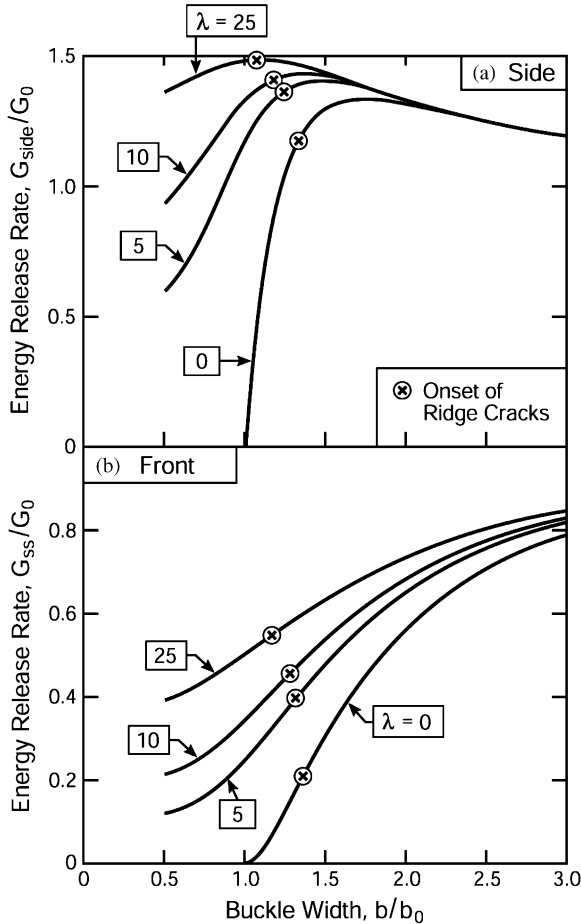


Fig. 8. Energy release rates along the sides and averaged over the front of straight-sided buckling delaminations without ridge cracks on flat and cylindrically curved substrates. These results apply to multilayer films and do not depend on M_0 . The smallest value of the normalized half-width of the delamination at which a deep ridge crack can form is indicated by \otimes (for a film with uniform properties and $M_0 = 0$).

A tensile stress acts across the intact interface between the film and the curved substrate when $R > 0$. Consequently, when the interface fails, the film separates from the substrate *even without buckling*. This is the origin of the non-zero energy release rates when $b/b_0 < 1$. The curvature also increases the peak value of G_{side} above that for the flat substrate.

3.3.3. Conditions for the formation of ridge cracks

Insight into the formation of ridge cracks that hinge at the bottom of the film can be obtained by considering a crack emerging from the top of a film subject to compression and bending (Fig. 9). A shallow crack has relatively little effect on the local bending stiffness. Consequently, a hinge only forms when the crack extends almost entirely through the film. The condition for a deep ridge crack will now be illustrated for a film with uniform properties.

The unbuckled film has residual compressive stress, N_0 , and moment, M_0 . In the buckled state at the ridge, the film supports the compressive stress and moment, N and $M = M_0 - Dw''(b)$, with the sign convention indicated in Fig. 9. Ridge cracking is suppressed by N and promoted by M , assuming both are positive. The occurrence of ridge cracking also depends on other factors, such as initial flaws and film toughness. Here, a lower bound on the cracking conditions of a single layer uniform film is derived under the assumption that the film has zero fracture toughness. The stress intensity factor for a crack (length a) emerging from the top of the film, subject to N and M (Fig. 9), is available (Tada et al., 2001). For $M/Nh > 1/6$ the stress at the top of the film becomes tensile and cracking becomes possible. For $1/6 < M/Nh < 1/2$, a crack length exists at which the stress intensity factor is zero, indicative of a crack within a film having negligible toughness. As $M/Nh \rightarrow 1/2$, the crack reaches the bottom of the film.

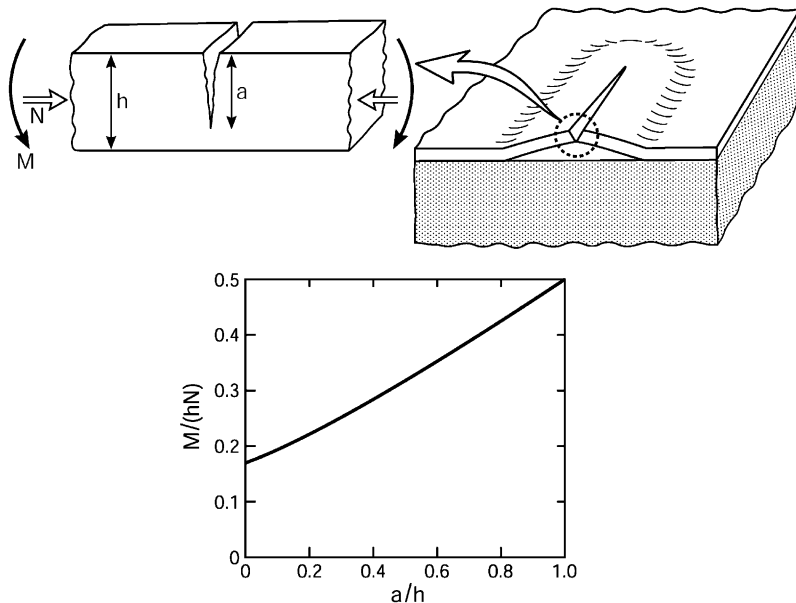


Fig. 9. Geometry of a ridge crack. The relation between the depth of the crack and combinations of resultant compression and bending moment at the center of the delamination for a uniform film with negligible toughness.

The condition $M/Nh = 1/2$ designates the condition for ridge cracks having sufficient depth such that a hinge forms about the bottom of the film, neglecting toughness of the film. For the flat substrate, the condition is attained when

$$\hat{M}_0 \left(\frac{b}{b_0}\right)^2 + \frac{1}{\sqrt{3}} \sqrt{\left(\frac{b}{b_0}\right)^2 - 1} = \frac{1}{2} \quad (24)$$

corresponding to $b/b_0 = 1.32$ if $M_0 = 0$. For the curved substrate the condition is

$$\hat{M}_0 \frac{N_0}{N} + \frac{\sqrt{\lambda}}{2\hat{y}_0} \frac{1}{p^2} \left(\frac{p}{\sin p} - 1\right) = \frac{1}{2}. \quad (25)$$

If $M_0 = 0$, deep ridge cracks are prohibited at b/b_0 below those indicated in Fig. 8. Positive values of the residual moment, M_0 , allow cracks to form at smaller b/b_0 .

3.4. Flat and curved substrates with ridge cracks

3.4.1. General solution

With a hinge at the bottom of the film (at $x = b$), the solution to Eq. (8) if $N > 0$ is

$$\frac{w(x)}{y_0} = \frac{b^2}{Ry_0} \left[\frac{1}{2} (\xi^2 - 2\xi) + \frac{\sin(p\xi)}{p} \right] + C(1 - \cos(p\xi)) \quad (26)$$

with $\xi = x/b$ and

$$\frac{\delta}{y_0} = \frac{b^2}{Ry_0} \left[-\frac{1}{2} + \frac{\sin p}{p} \right] + C(1 - \cos p), \quad (27)$$

$$\frac{\alpha b}{y_0} = \frac{b^2}{Ry_0} \cos p + Cp \sin p, \quad (28)$$

where p is given in Eq. (20) and

$$C = \frac{1}{\cos p} \left[\frac{b^2}{Ry_0} \left(\frac{\sin p}{p} - \frac{1}{p^2} \right) + \frac{1}{p^2} \frac{M_0 b^2}{Dy_0} - 1 \right]. \quad (29)$$

Then, Eq. (9) becomes

$$1 - \frac{N}{N_0} = \frac{1}{\pi^2} \left(\frac{b_0}{b}\right)^2 \left\{ -\frac{\alpha b}{y_0} \hat{y}_0^2 + \lambda \left[-\frac{1}{6} + \frac{1}{4} \left(1 + \frac{\sin 2p}{2p}\right) \right] + \sqrt{\lambda} \hat{y}_0 \frac{C}{4} (1 - \cos 2p) + \frac{(\hat{y}_0 Cp)^2}{4} \left(1 - \frac{\sin 2p}{2p}\right) \right\}. \quad (30)$$

The energy release rates are

$$\frac{G_{\text{side}}}{G_0} = \left(1 - \frac{N}{N_0}\right)^2 + \frac{\hat{y}_0^2}{\pi^4} \left(\frac{b_0}{b}\right)^2 \left(\frac{b^2}{Ry_0} + p^2 C\right)^2, \quad (31)$$

$$\begin{aligned} \frac{G_{ss}}{G_0} = & 1 - \left(\frac{N}{N_0}\right)^2 + \frac{2}{\pi^2} \left(\frac{b}{b_0}\right)^2 \hat{y}_0^2 \hat{M}_0 \left(\frac{\alpha b}{y_0}\right) - \frac{\lambda_0}{\pi^4} \left[1 + 2(\cos p - 1) + \frac{p^2}{2} \left(1 - \frac{\sin 2p}{2p}\right) \right] \\ & - \frac{\sqrt{\lambda_0}}{\pi^4} \hat{y}_0 C \left(\frac{b_0}{b}\right)^2 \left[2p \sin p + \frac{p^2}{2} (\cos 2p - 1) \right] - \frac{1}{2\pi^4} \hat{y}_0^2 C^2 p^4 \left(\frac{b_0}{b}\right)^4 \left(1 + \frac{\sin 2p}{2p}\right). \end{aligned} \tag{32}$$

The relative mode II to mode I [$\psi = \arctan(K_{II}/K_I)$] along the sides of the delamination increases as its width increases, and the mode-dependence of the interface toughness plays a significant role in limiting the delamination width. General results for the mode mix, ψ , are not available for multilayer films. To display the effect of ridge cracking, we present selected results for single layer films. These are based on the expressions for the change in resultant stress and bending moment at the edge of the buckled film (Hutchinson and Suo, 1992). For the ridge-cracked film analyzed above the result can be expressed as

$$\tan \psi = \frac{\sqrt{12} + A \tan \omega}{-\sqrt{12} \tan \omega + A} \tag{33}$$

with

$$A = \frac{2y_0(N_0 - N)}{Dw''(0)} = 2\pi^2 \left(\frac{b}{b_0}\right)^2 \left(1 - \frac{N}{N_0}\right) \left(\frac{b^2}{Ry_0} + Cp^2\right)^{-1}.$$

When there is no elastic mismatch between the film and the substrate, $\omega = 52.1^\circ$.

When $M_0 > 0$ the resultant stress in the buckled state can become tensile (i.e., $N < 0$). The formulae above apply if $N < 0$ when the following changes are made. With

$$q \equiv b\sqrt{-N/D} = \pi(b/b_0)\sqrt{-N/N_0}, \tag{34}$$

let $p = \sqrt{-1}q \equiv iq$ such that $p^2 = -q^2$, $\sin p = i \sinh q$, $\cos p = \cosh q$, $\sin 2p = i \sinh 2q$, etc. By replacing the terms involving p by q , real expressions emerge, which analytically extend the formulae into the range of negative N . The above formulae also apply to flat substrates in the limit, $R \rightarrow \infty$.

3.4.2. Effects of ridge cracks and residual moment for flat substrates

Three sets of release rate for delaminations on flat substrates are plotted in Fig. 10. (a) Films with no ridge cracks (from Eq. (17)). (b) Films with ridge cracks modeled by a hinge at $y = y_0$ (from Thouless (1993); albeit that this is an unrealistic model, since it implies interpenetration of material below the hinge). (c) Films with ridge cracks modeled by a hinge at $y = 0$ (from Eqs. (29) through (33)). The accompanying plots for the mode mix at the sides apply only to single layer films having no elastic mismatch with the substrate ($\omega = 52.1^\circ$). In these examples, $M_0 = 0$ for the films with ridge cracks. The difference between placing the hinge at $y = 0$ and $y = y_0$ highlights the appreciable error incurred when the latter assumption is used. The fact that G_{side}/G_0 appreciably exceeds unity will be discussed below.

Note that, when ridge cracking occurs, the half-width, b , of the delamination at which the sides attain mode II is reduced. The implication is that ridge-cracked delaminations should be significantly narrower than uncracked delaminations, consistent with the observations made on DLC films (Fig. 2d).

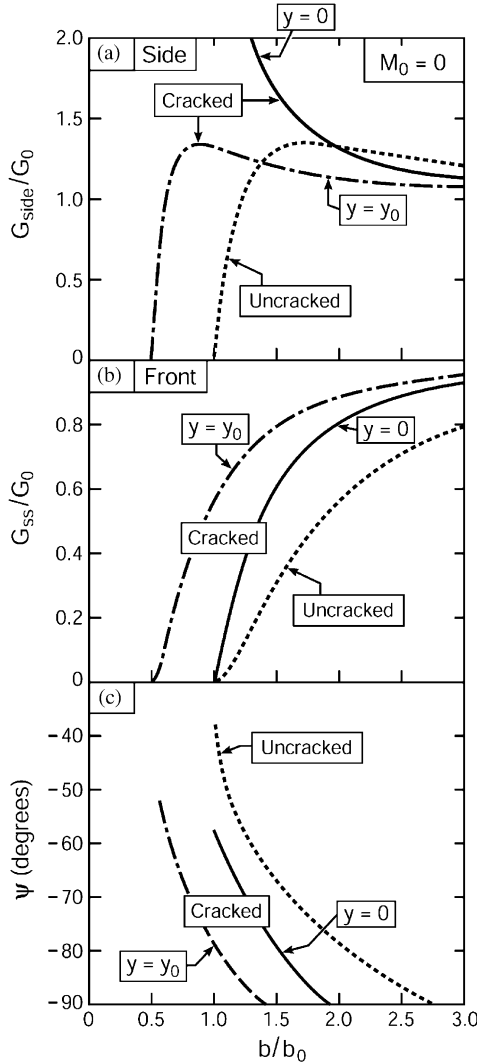


Fig. 10. Energy release rates (a and b) and mode mix (c) for multilayer buckle delaminations on a flat substrate, with and without ridge cracks. The results for the ridge cracks have $M_0 = 0$, while the results for the uncracked delamination are independent of M_0 . Two cases for ridge cracks are shown: (i) modeled by a hinge half way through the film thickness and (ii) modeled by a hinge at the bottom of the film. The mode mix applies to a uniform film.

The influence of the residual moment for ridge-cracked buckles (hinged about $y = 0$) on flat substrates is shown in Fig. 11, computed using Eqs. (29) through (33). Attention is focused on cases with $M_0 \geq 0$. The results have been plotted over the range in which the delamination has a positive mode I on the sides. It is striking that (unlike G_{side}) G_{ss} has a strong dependence on M_0 : approaching G_T in Eq. (14) (Fig. 11b) as the delamination width approaches mode II on the sides.

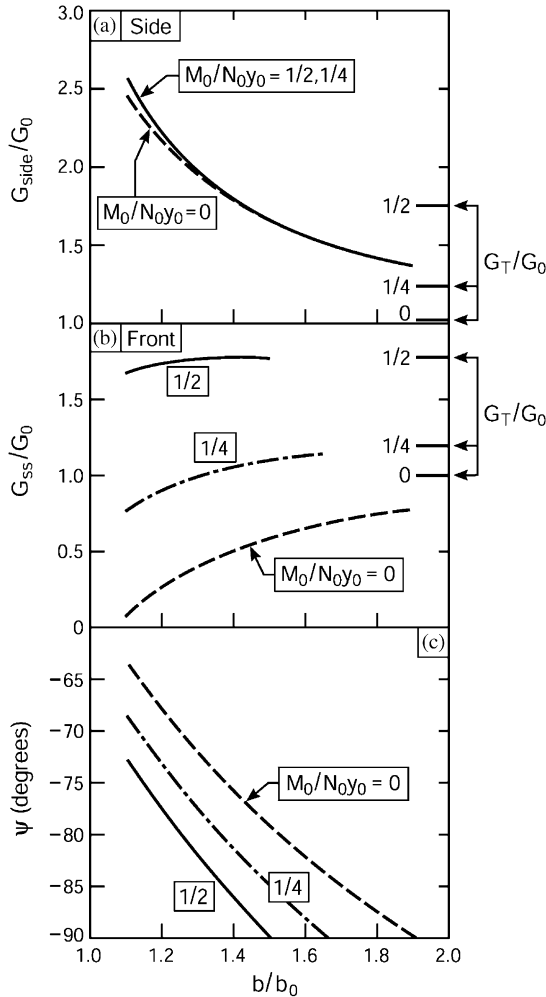


Fig. 11. Energy release rates and mode mix for ridge-cracked delaminations on a flat substrate in the presence of a residual moment M_0 . The mode mix applies only to a uniform film.

Paradoxically, at small b/b_0 , G_{side} exceeds G_T . This is not a violation of energy conservation. Indeed, even in the classical result for the uncracked film (Fig. 10), the peak G_{side} is about 50% larger than G_0 . Three features of the energetics clarify the paradox. (a) Energy conservation considerations based on Eq. (13) dictate that $G_{\text{ss}} \leq G_T$ (or $G_{\text{ss}} \leq G_0$ if the film is uncracked): all the present results satisfy this requirement. (b) The energy release rates at the front and sides are related by $G_{\text{ss}} = b^{-1} \int G_{\text{side}} db$ (or, equivalently, $G_{\text{side}} = G_{\text{ss}} + b dG_{\text{ss}}/db$). Thus, while the integral of G_{side} must be less than bG_T , G_{side} itself can be large when dG_{ss}/db is large. The plots of G_{side} and G_{ss} for planar substrates, over the entire range of b/b_0 (Fig. 10), provide the clearest illustration. (c) Substrate curvature enhances G_{side} at smaller b/b_0 , because of the tensile stress acting across the interface. This contribution is not explicitly related to the energy in the film.

3.4.3. Effects of ridge cracks and residual moment for curved substrates

The effects of ridge cracks on the energy release rates for curved substrates are demonstrated on Figs. 12 and 13. Note that substrate curvature lowers the normalized half-width, b/b_0 , at which the delamination along the sides becomes mode II. Positive M_0 lowers it even further, but does not otherwise significantly influence G_{side} . The range of b/b_0 over which ridge-cracked buckles are admissible is limited at small b/b_0 by conditions for the onset of ridge cracking (Fig. 8), and at large b/b_0 by the attainment of pure mode II along the sides ($|\psi| = 90^\circ$).

The equilibrium profile of the buckle delamination is intimately linked to the strong mode-dependence of interface toughness, $\Gamma_{int}(\psi)$ (Hutchinson and Suo, 1992). Recall that mode II increases sharply with b along the sides, and that this trend is further promoted by ridge cracking. Consequently, the width of the delamination, which is determined by

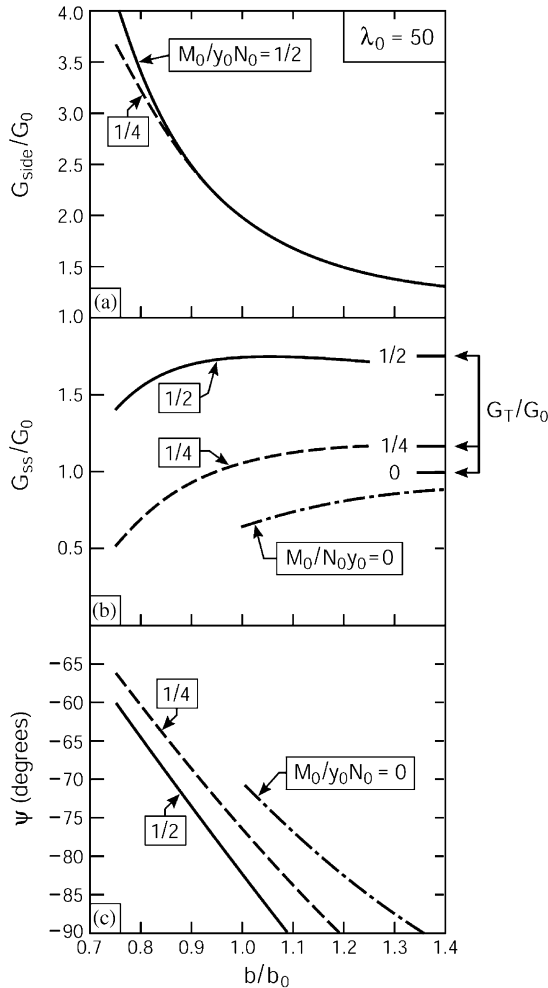


Fig. 12. Energy release rates and mode mix for ridge-cracked delaminations on a curved substrate (with $\lambda_0 = 50$) in the presence of a residual moment M_0 . The mode mix applies only to a uniform film.

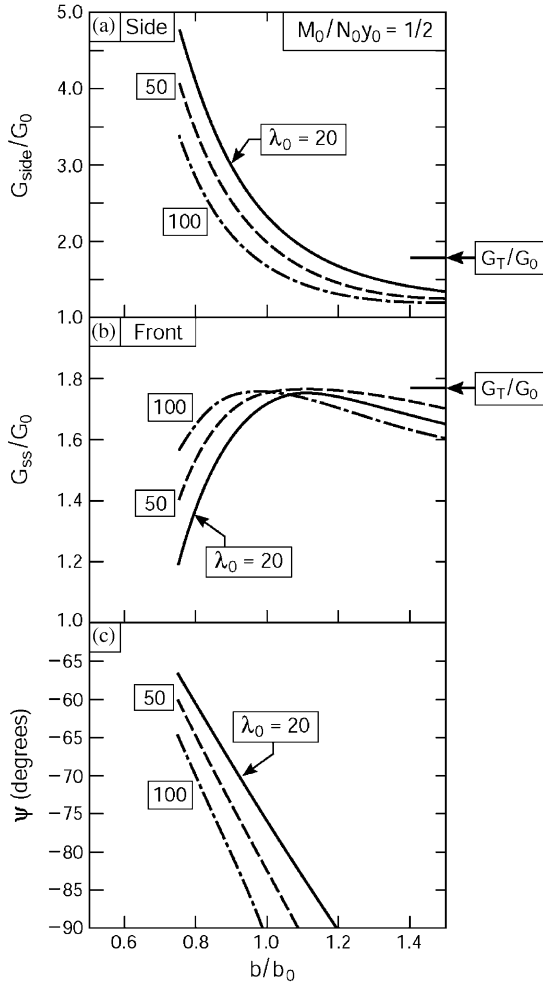


Fig. 13. Energy release rates and mode mix for ridge-cracked delaminations on substrates with various normalized curvatures in the presence of a residual moment M_0 .

$G_{\text{side}} = \Gamma_{\text{int}}(\psi)$, will usually be attained at near-mode II conditions. However, the mode mix along the curved front has a significant component of mode I. While there are no general results for curved substrates, we recall that, for uniform films on flat substrates, along the front $-70^\circ < \psi < -40^\circ$ over the relevant range of b/b_0 (Moon et al., 2002b). Thus, usually, equilibrium delamination configurations have G_{ss} much smaller than G_{side} .

3.5. The inverse algorithm

The objective is to infer the residual stress and moment resultants (N_0 and M_0) and the energy release rates, G_{side} and G_{ss} , given three measurements: the buckling deflection, δ , the slope, α , at the location of the central ridge crack, as well as the delamination half-width, b ,

all measured well behind the propagating front. The following quantities are assumed known: R, S, D and y_0 . The system of Eqs. (27)–(30), is too nonlinear and implicit to allow anything other than a numerical algorithm.¹ The ensuing procedure is based on the unapproximated equations listed above.

Step I: Determine p , and then $N = D(p/b)^2$, from the nonlinear equation

$$\frac{\delta}{1 - \cos p} - \frac{\alpha b}{p \sin p} = \frac{b^2}{R} \left[\frac{1}{p \sin p} - \frac{1}{2(1 - \cos p)} \right].$$

This assumes N is positive. If there is no solution with $0 < p < \pi$, look for solutions with negative N by converting the governing equations using $q \equiv b\sqrt{-N/D}$ as described above and look for q that satisfies the converted equation.

Step II: Evaluate C using

$$C = \frac{\delta/y_0}{1 - \cos p} - \frac{b^2}{Ry_0} \frac{(-1/2 + \sin p/p)}{1 - \cos p}.$$

Step III: Evaluate $M_0 = (Dy_0/b^2)p^2(C \cos p + 1)$.

(In subsequent steps, M_0 only influences G_{ss} .)

Step IV: Evaluate N_0 using

$$N_0 = N + \frac{D}{b^2} \left\{ -\frac{\alpha b}{y_0} \hat{y}_0^2 + \lambda \left[-\frac{1}{6} + \frac{1}{4} \left(1 + \frac{\sin 2p}{2p} \right) \right] \right. \\ \left. + \sqrt{\lambda} \hat{y}_0 \frac{C}{4} (1 - \cos 2p) + \frac{(\hat{y}_0 Cp)^2}{4} \left(1 - \frac{\sin 2p}{2p} \right) \right\}.$$

Step V: Evaluate G_0 using Eq. (11), G_{side} using Eq. (31) and G_{ss} using Eq. (32). If the film properties can be regarded as nominally uniform, ψ can be evaluated using Eq. (33) where b_0 is obtained from Eq. (11).

The fact that M_0 is not needed in the evaluation of N_0 , G_0 and G_{side} is significant because (as already noted) G_{side} is relatively insensitive to M_0 (Figs. 11a and 12a). The accuracy and robustness of the approach has been checked for several cases using exact solutions. It will be illustrated next for a diamond-like carbon film on a flat substrate and thermal barrier layers on curved substrates.

4. Application of the inverse algorithm

4.1. DLC film on a flat glass substrate

When DLC films are deposited on a flat glass substrate, they may simultaneously exhibit telephone cord and straight-sided ridge-cracked buckle delaminations (Fig. 2d). A transverse section through the ridge-cracked cut with a focused ion beam (Fig. 2e) reveals the profile and the extent of the delamination. The DLC film has $E \cong 50$ GPa and $\nu = 0.3$ (Cho et al., 2004) and for the present case, $h = 380$ nm. The half-width of the delamination is, $b = 6.4$ μm , and the buckle amplitude (measured with an atomic force microscope) is, $\delta = 1.4$ μm . The angle α was not measured. Under the assumption the film experiences a

¹Several schemes were attempted, but none proved adequate. The most promising entailed linearizing the solution for $w(x)$ with respect to N/N_0 and then using it in conjunction with the unapproximated Eq. (9). However, even this approach was not sufficiently accurate even when N/N_0 was small.

relatively small residual moment, the theory gives $p \cong \pi/2$ and $\alpha \cong (\pi/2)\delta/b \cong 20^\circ$. Based on these quantities, the inverse algorithm gives

$$\sigma_0 = 1.0 \text{ GPa}, \quad G_0 = 4.1 \text{ Jm}^{-2}.$$

The inferred interface toughness are:

$$\Gamma_{\text{int}}(\psi \approx 90^\circ) \equiv G_{\text{sides}} = 4.7 \text{ Jm}^{-2},$$

$$\Gamma_{\text{int}}(\psi \approx 60^\circ) \equiv G_{\text{ss}} = 3.8 \text{ Jm}^{-2}.$$

The fidelity of these results is assessed by comparison with independent measurements. The residual compression in the film has been obtained by wafer curvature techniques (Lee et al., 1994) as: $1.0 \leq \sigma_0 \leq 1.3 \text{ GPa}$. The mode II interface toughness has been inferred from measured characteristics of the telephone cord delaminations (Moon et al., 2002a) as: $4 \leq \Gamma_{\text{int}} \leq 7 \text{ Jm}^{-2}$. The consistency with the present results lends credence to the ridge-crack analysis.

Note that the present estimate of the normalized residual moment ($M_0/y_0N_0 = 0.026$) indicates that the effect of the residual moment is negligible, consistent with the assumption in assigning α . The normalized half-width, $b/b_0 = 2.7$, implies the interface crack along the sides is subject to pure mode II (Fig. 10).

4.2. Thermal barrier bilayer on cylindrical substrate

For the ridge-cracked thermal barrier bi-layer (Fig. 6) the thin alumina layer (layer #1) has $h_1 = 2.3 \mu\text{m}$, $E_1 = 400 \text{ GPa}$ and $\nu_1 = 0.2$. Layer #2 is the porous zirconia thermal barrier ($h_2 = 140 \mu\text{m}$). Its modulus, which is denoted by E_2 , is not certain; we will examine its effect by considering E_2 as a parameter lying in the range from 10 to 60 GPa (Johnson et al., 1998). Its Poisson ratio will be taken as $\nu_2 = 0.2$, but the results are not sensitive to this parameter. As reported in Section 2, $R = 6 \text{ mm}$, $b = 1.2 \text{ mm}$, $\delta = 60 \mu\text{m}$ and $\alpha = 2.6^\circ$.

Based on the above inputs, the quantities ascertained from the inverse algorithm are plotted in Figs. 14a–c, as a function of the unknown in-plane modulus of the TBC. To obtain these results, the stresses in the TGO and TBC layers are assumed to be spatially uniform, enabling simultaneous determination from N_0 and M_0 . Since M_0 is small ($M_0/y_0N_0 \leq 1$), G_T is only slightly larger than G_0 (Fig. 14b). The energy release rate at the front G_{ss} (Fig. 14b) is well below G_T , whereas that at the sides is much larger (not plotted); consistent with the small $b/b_0 \cong 0.7$. Incorporating the measured stress in the TGO ($\sigma_{\text{TGO}} = -4.2 \text{ GPa}$) infers that the TBC has modulus, $E_2 \approx 50 \text{ GPa}$, within the range obtained by independent measurements (Johnson et al., 1998). Using this modulus gives:

$$\Gamma_{\text{int}}(\psi \approx 80^\circ) \equiv G_{\text{sides}} \cong 300 \text{ Jm}^{-2},$$

$$\Gamma_{\text{int}}(\psi \approx 60^\circ) \equiv G_{\text{ss}} \cong 75 \text{ Jm}^{-2}.$$

Values in this range have been measured in mode I for diffusion-bonded $\text{Al}_2\text{O}_3/\text{Ni}$ (alloy) interfaces (Evans et al., 1999). However, at the higher values, the interface cracks experience quite large crack opening due to plastic blunting (Gaudette et al., 1997; Zhang et al., 2003), contrasting with the small crack opening characterizing the delamination of the present interface (Fig. 3). Consequently, the fidelity of the large values, especially that at the sides, requires further deliberation. Given the irregular trajectory of the interface crack (Fig. 3), there will be appreciable friction and asperity interaction when the loading

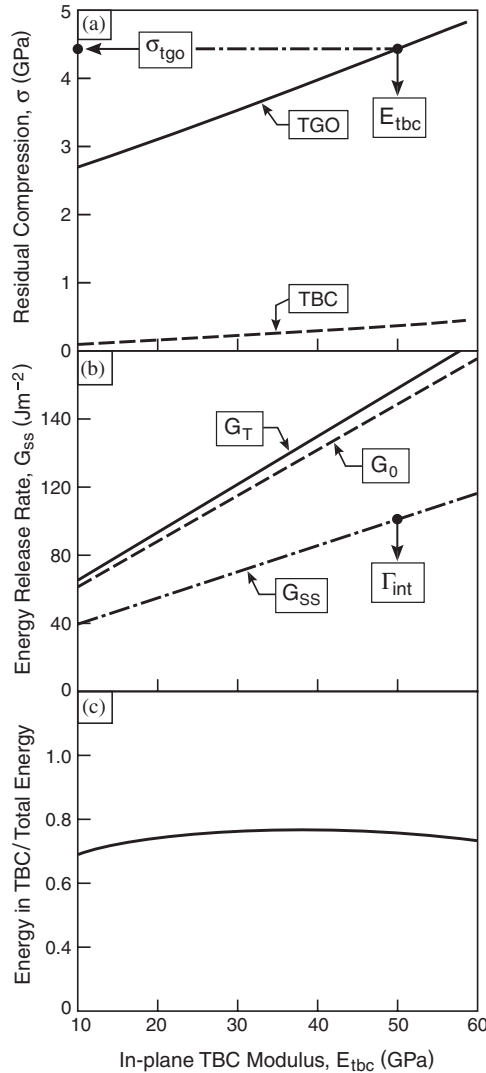


Fig. 14. Results obtained for thermal barrier bilayers using the inverse algorithm. (a) The trend in residual compression in the two layers with in-plane elastic modulus of the TBC layer. Incorporating the stress measured in the TGO (Fig. 6) implies a modulus, $E_{tbc} \approx 50$ GPa. (b) Trends in the steady-state energy release rate and the energies/area in the unbuckled bilayer with TBC modulus. (c) The ratio of the elastic energy in the TBC layer to the total energy in the unbuckled bilayer.

approaches mode II, so it is perhaps a reasonable value. The appreciably lower value inferred from the energy release rate along the propagating front (at $\psi \approx 60^\circ$) would be consistent with a strong influence of mode mix on the interface toughness. A concern, however, is that the inferred toughness values are erroneously high due to the nonlinear elasticity of the TBC: recalling that the energy in each layer is computed based on linear stress–strain behavior. There is evidence that the incremental modulus of the TBC layer diminishes as the compressive stress is lowered (Johnson et al., 1998) due to the opening of

inter-columnar gaps, suggesting that the elastic energy stored in the layer (Fig. 14c) has been overestimated. In order to resolve this concern, and before a fidelity can be attached to the inferred toughness, new measurements of the stress dependence on the TBC modulus are needed.

5. Conclusion

Motivated by observations of ridge-cracked buckles on curved thermal barrier systems, the mechanics governing the energy release rates at the sides, G_{sides} and along the front, G_{ss} , have been determined. It is shown that ridge cracks and substrate curvature profoundly affect both energy release rates, but especially G_{sides} . The consequences are that buckles with ridge cracks and on convex substrates have appreciably smaller width than uncracked buckles on flat substrates. The residual moment can also affect the width when the buckle has a ridge crack. The analysis has been developed in a sufficiently general form that the results are applicable to multilayers.

An inverse algorithm has been developed with the remarkable feature that (whether cracked or uncracked) measurements of the buckle profile allow simultaneous determination of two separate quantities: especially the interface toughness and the stress in the film (if the elastic properties are known), or the interface toughness and the modulus (if the stresses are known). The fidelity of the algorithm has been assessed by conducting measurements on ridge-cracked buckles in DLC films on planar glass substrates and comparing the inferred values of both the interface toughness and the stress in the film with independently measured values.

The method has been applied to thermal barrier bilayers (TGO and TBC) on curved superalloy substrates. In this case, the stress in the TGO is known from independent measurements, while the interface toughness and the modulus of the TBC layer are unknown. The results infer a reasonable TBC modulus, but the implied toughness at the sides and the front are very different and unexpectedly large for such an interface. An assessment of the toughness has highlighted dependence of the fidelity of the algorithm on the elastic linearity of the layers. However, TBCs have a stress-dependent modulus, with the consequence that the energy stored in this layer could be appreciably smaller than that calculated for a linear material. The fidelity of the toughness measurements thus awaits detailed measurements of the stress-dependent elastic properties of the TBC.

References

- Cho, S.-J., Chung, J.-W., Lee, K.-R., 2004. Characterization of the mechanical properties of diamond-like carbon films. *Diamond Relat. Mater.* 14, 1270–1276.
- Clarke, D.R., Levi, C.G., 2003. Materials design for the next generation thermal barrier coatings. *Annu. Rev. Mater. Res.* 33, 383–417.
- Evans, A.G., Hutchinson, J.W., Wei, Y., 1999. Interface adhesion: effects of plasticity and segregation. *Acta Mater.* 47, 4093–4113.
- Evans, A.G., Mumm, D.R., Hutchinson, J.W., Meier, G.H., Pettit, F.S., 2001. Mechanisms controlling the durability of thermal barrier coatings. *Prog. Mater. Sci.* 46 (5), 505–553.
- Freund, L.B., Suresh, S., 2004. *Thin Film Materials: Stress, Defect Formation and Surface Evolution*. Cambridge University Press, Cambridge.
- Gaudette, F., Suresh, S., Evans, A.G., Dehm, G., Rühle, M., 1997. The influence of chromium additions on the toughness of γ -Ni/ α -Al₂O₃ interfaces. *Acta Mater.* 45, 3503–3514.

- Hutchinson, J.W., 2001. Delamination of compressed films on curved substrates. *J. Mech. Phys. Solids* 50, 1847–1864.
- Hutchinson, J.W., Suo, Z., 1992. Mixed mode cracking in layered materials. *Adv. Appl. Mech.* 29, 63–191.
- Johnson, C.A., Ruud, J.A., Bruce, R., Wortman, D., 1998. Relationships between residual stress, microstructure and mechanical properties of electron beam-physical vapor deposition thermal barrier coatings. *Surf. Coat. Technol.* 108–109, 80–85.
- Lee, A., Clemens, B.M., Nix, W.D., 2004. Stress induced delamination methods for the study of adhesion of Pt thin films to Si. *Acta Mater.* 52, 2081–2093.
- Lee, K.-R., Baik, Y.-J., Eun, K.Y., Han, S., 1994. Precursor effect on the structure and properties of diamond-like carbon films. *Diam. Relat. Mater.* 3, 1230–1234.
- Levi, C.G., 2004. Emerging materials and processes for thermal barrier systems. *Curr. Opin. Solid St. M.* 8, 77–91.
- Lipkin, D.M., Clarke, D.R., 1996. Measurement of the stress in oxide scales formed by oxidation of aluminum containing alloys. *Oxid. Met.* 45, 267–280.
- Ma, Q., Clarke, D.R., 1993. Stress measurement in single-crystal and polycrystalline ceramics using their optical fluorescence. *J. Am. Ceram. Soc.* 76, 1433–1440.
- Moon, M.-W., Chung, J.-W., Lee, K.-R., Oh, K.H., Wang, R., Evans, A.G., 2002a. An experimental study of the influence of imperfections on the buckling of compressed thin films. *Acta Mater.* 50, 1219–1227.
- Moon, M.-W., Jensen, H.M., Oh, K.H., Hutchinson, J.W., Evans, A.G., 2002b. The characterization of telephone cord buckling of compressed thin films on substrates. *J. Mech. Phys. Solids* 50, 2355–2377.
- Parry, G., Colin, J., Coupeau, C., Foucher, F., Cunetiere, A., Grilhe, J., 2005. Effect of substrate compliance on the global unilateral post-buckling of coatings: AFM observations and finite element calculations. *Acta Mater.* 53, 441–447.
- Stiger, M.J., Yanar, N.M., Topping, M.G., Pettit, F.S., Meier, G.H., 1999. Thermal barrier coatings for the 21st century. *Z. Metallkd.* 90, 1069–1078.
- Tada, H., Paris, P.C., Irwin, G.R., 2001. *The Stress Analysis of Cracks Handbook*. ASME Press, New York.
- Thouless, M.D., 1993. Combined buckling and cracking of films. *J. Am. Ceram. Soc.* 76, 2936–2938.
- Xu, T., Faulhaber, S., Mercer, C., Maloney, M., Evans, A.G., 2004. Observations and analyses of failure mechanisms in thermal barrier systems with two phase bond coats based on NiCoCrAlY. *Acta Mater.* 52, 1439–1450.
- Zhang, W., Smith, J.R., Wang, X.-G., Evans, A.G., 2003. Influence of sulfur on the adhesion of the nickel/alumina interface. *Phys. Rev. B* 67 (24), 245414.